The Effect of Cooling Rate on the Microstructures Formed during Solidification of Ferritic Steel

N.H. PRYDS and X. HUANG

This article describes in detail the effect of cooling rate on the microstructure of a low-carbon Fe-12 pct Cr alloy. The alloy was prepared using a relatively simple technique, *i.e.*, rapid cooling of the melt in a copper wedge mold. The dependence of microstructure on the cooling rate (~40 to 10^5 K/s) has been determined by X-ray diffraction (XRD), microhardness measurement, optical microscopy (OM), and transmission electron microscopy (TEM). It has been found that the matrix structure over a large cooling rate range is composed of columnar ferrite grains, the size of which decreases with increasing cooling rate. Precipitation of second phases has been observed at either the ferrite grain boundaries or within the ferrite grains. The former takes place along the entire wedge sample, whereas the latter characterizes a region 12 mm away from the tip of the wedge sample. The essential structure of the grain boundary precipitates was identified as martensite, which is a transformation product of austenite precipitated at high temperatures. Retained austenite was identified at the tip region as isolated particles (<4 μm). The precipitates within the ferrite grains appeared as planar colonies consisting of two sets of needles. The density of these precipitates increases with increasing the cooling rate while their size decreases. Characteristic precipitate-free zones (PFZs) at the ferrite grain boundaries were observed and are discussed.

I. INTRODUCTION

THE commercial corrosion resistant Fe-Cr-Ni alloys ($>$11.5 pct Cr) containing very little Ni ($<$2.5 pct) are generally termed martensitic or ferritic stainless steels. The composition of the alloys is one of the major factors that determines the amount of martensite/δ-ferrite formed; *e.g.*, austenite forming elements (*e.g.*, C, N, and Ni) promote the formation of austenite phase, while ferrite-forming elements (*e.g.*, Cr, Mo, and V) discourage austenite formation.[1–4] In the ferritic stainless steel, the austenite has often been observed to precipitate at the δ-ferrite grain boundaries and transform into martensite on cooling to room temperature. The morphologies of the grain boundary precipitates have been earlier examined and classified for isothermally transformed alloy steel by Dubé *et al.*[5] for ferrite morphology and later modified by Aaronson[6] for ferrite and cementite morphologies. Based on these investigations, it has been suggested that the morphologies of the grain boundary precipitates consist of[6] (1) allotriomorph, (2) primary and secondary sideplates (sideneedles), (3) primary and secondary sideteeth, (4) idiomorphs, (5) intergranular Widmanstätten plates, and (6) massive structure. Recently, three-dimensional analyses were conducted to determine more precisely the classification of the precipitates.[7] The results of these investigations indicated that only dendritic grain boundary precipitates and Widmanstätten precipitate morphologies exist and that the intergranular precipitates were not observed. The morphology can strongly affect the mechanical properties of the alloy. Knowledge of the morphology formation can therefore provide a way of controlling and optimizing the mechanical properties of the alloy.[8]

During the last 3 decades, a considerable effort has been devoted to study the effect of rapid solidification on Fe-base alloys mainly due to the inherent technical importance of this class of materials.[9–12] It is known that rapid solidification processing can result in microstructure refinement, formation of metastable phases and morphological changes. Although rapid solidification enables production of more uniform and refined microstructure in comparison with conventional solidification, the understanding of the local inhomogeneity of the products during rapid solidification and their influence on the subsequent precipitation processes is also of technical importance. In recent studies, the microstructural development has been characterized in 12 pct Cr stainless steels produced by different rapid solidification processes, namely, gas atomizing, melt spinning, and laser surface remelting, showing that the solidification conditions have a strong effect on the structures that are formed.[13,14]

The present study was undertaken to obtain a detailed understanding of the effect of cooling rate on a low-carbon Fe-Cr alloy. A wedge chill casting technique has been used to prepare samples that experience a large cooling rate variation. The cooling rates were then determined at different positions in the mold. Based on these measurements and detailed observations of microstructures, the relation between the cooling rate and the resulting microstructures was determined and is discussed in the text. Finally, a systematic view of the evolution of the microstructure as a function of cooling rate is proposed.

II. EXPERIMENTAL PROCEDURE

The investigated low-carbon Fe-Cr steel was prepared by induction melting under an argon atmosphere and then casting the alloy into a wedge-shaped copper mold. The composition of the prepared sample was then analyzed by chemical analysis (Table I). The wedge-shaped copper mold was used as it provides a wide range of cooling rates for the same

---

N.H. PRYDS and X. HUANG, Senior Scientists, are with the Materials Research Department, Risø National Laboratory, DK-4000 Roskilde, Denmark.

Manuscript submitted February 18, 2000.

Table I. Compositions of the Alloy (in Weight Percent)

Element	
Cr	11.3
Mo	0.87
Mn	0.36
Ni	0.77
C	0.045
V	0.25
N	145 ppm
Fe	bal

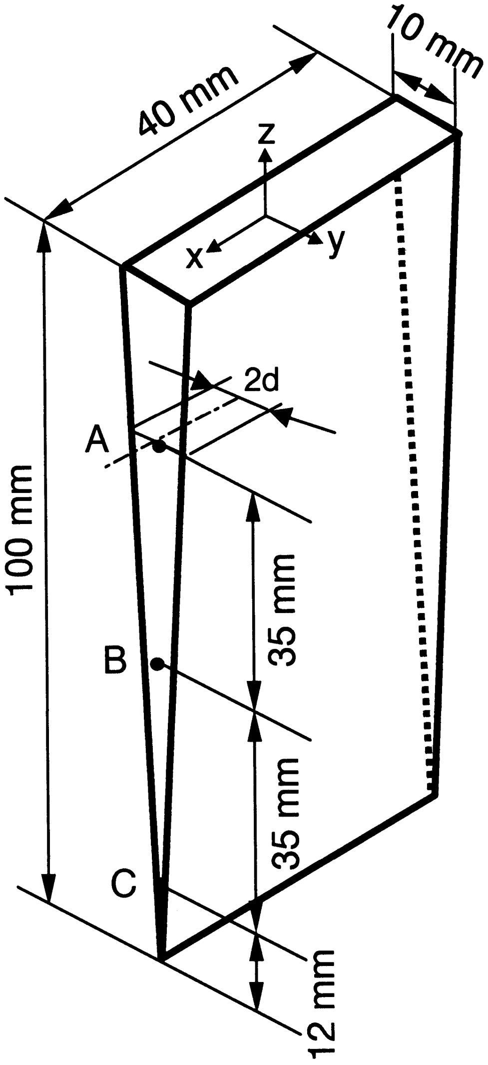

Fig. 1—Schematic illustration of the wedge-formed sample. The locations in which the thermocouples were inserted are marked "A," "B," and "C."

alloy composition. Figure 1 shows the final shape of the sample. In order to measure the temperature and the time during the solidification, thermocouples were introduced at different positions within the wedge mold (Figure 1). The size of the thermocouple wires was chosen as 0.3 mm in order to achieve a good transient response during the measurements (type R, Pt-13 pct Rh/Pt). From the temperature and time measurements, the cooling rates throughout the solidification temperature range were determined at the measurement positions. The cooling rate ($\dot{T}$) was then plotted as a function of d (half-thickness of the wedge, refer to the z-y plane in Figure 1), and the following empirical relationship was found:

$$\dot{T} = \frac{(926 \text{ K mm}^2/\text{s})}{d^2} \qquad [1]$$

Different sections of the wedge-formed samples, normal to the x or y axes (Figure 1), were mounted in a conductive resin, mechanically polished, and then etched using a solution containing 1 to 2 g NH_2SO_3H, 0.5 to 1 g NH_4FHF, and 3 g $K_2S_2O_5$ in 100 mL distilled water. The samples were studied with an optical microscope equipped with image analysis.

The microhardness of the wedge-formed samples along a line normal to the x-y plane was determined using a Knoop hardness test with a testing load of 100 g.

X-ray diffraction (XRD) was performed using Bragg–Brentano geometry with a STOE&CIE θ/θ powder diffractometer, equipped with an energy dispersive Kevex detector. The radiation used was Cu K_α. The measurements were made to determine the phases at different sections of the wedge-formed samples (normal to the x-y plane, Figure 1).

Thin foils for transmission electron microscopy (TEM) observations were taken from different parts of the wedge-formed sample. The foils were prepared using 20 pct $HClO_4$ in methanol at −15 °C by a twin-jet polishing apparatus. The TEM observations were conducted on a JEOL-2000FX electron microscope operating at 200 kV.

III. RESULTS

A. *Constitution*

Figures 2(a) through (c) show the XRD patterns obtained from three locations of the wedge sample subjected to three different cooling rates, *i.e.*, 75, 7.5×10^3, and 4.1×10^4 K/s, which correspond to distances of 70, 7, and 3 mm from the tip of the wedge. The diffraction profile in Figure 2(a) is identified as ferrite. However, as will be seen later, within these regions, the structure consists also of martensite at the grain boundaries of the matrix, *i.e.*, the ferrite. In view of the low-carbon content in the present steel, both the martensite and ferrite are expected to have approximately the same lattice parameters. Therefore, it is impossible to distinguish between them by using XRD. Low-temperature α-ferrite formation was excluded because the rapid rate of cooling retained the high-temperature δ-ferrite to room temperature. As shown by XRD, there is no phase change at the upper part of the sample. However, at the tip region, besides the diffraction peaks corresponding to the ferrite/martensite, extra peaks are observed. The peaks marked (γ) are found to correspond to austenite, while the phase corresponding to the peaks labeled "P" is carbide but could not be completely identified by these experiments as the number of diffraction peaks is limited. However, the peaks labeled "P" are found to be consistent with cementite. A complete phase determination of the precipitates has recently been made on the basis of a series of selected area electron diffraction patterns,[15] and the precipitates have been identified as orthorhombic cementite M_3C.

B. *Microhardness*

Figure 3 shows the microhardness measurements taken along the wedge sample, *i.e.*, the z-axis is the distance from

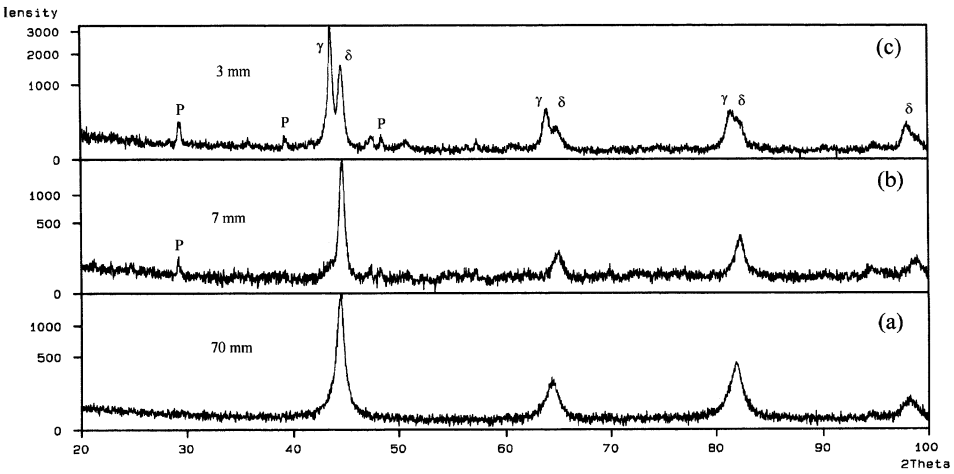

Fig. 2—(*a*) through (*c*) XRD patterns obtained at different locations along the direction parallel to the *z*-axis showing the formed phases; (a) 3 mm, (b) 7 mm, and (c) 70 mm. Key to symbols: (P) carbide, (δ) ferrite, and (γ) austenite.

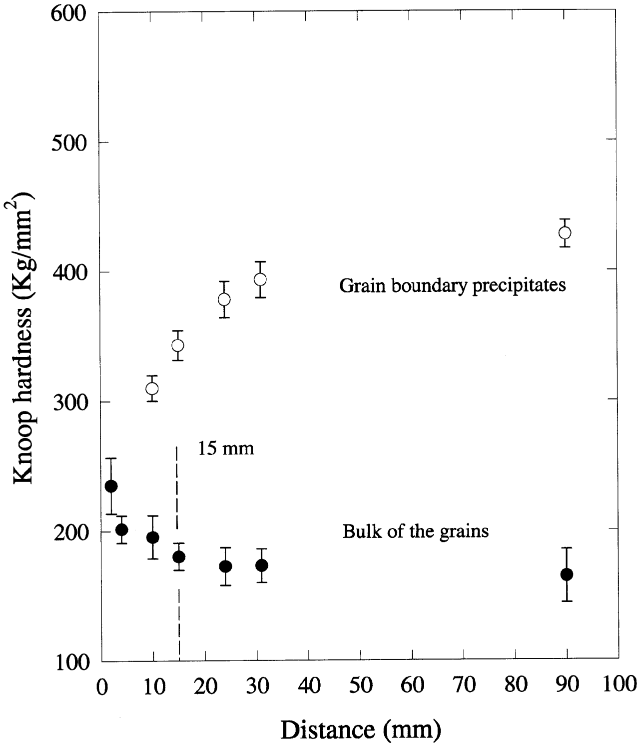

Fig. 3—Microhardness measurements along the wedge-formed sample. Key to symbols: (○) measured at the grain boundary precipitates and (●) measured at the grain bulk. The error bar represents the standard deviation.

the tip to the top of the wedge (100 mm), in the grain boundary interior, and at the grain boundaries precipitate. Since the microstructure affects the microhardness measurements, these measurements provide a tool for evaluating the formed microstructures. The microhardness of the bulk δ ferrite grains shows decreasing values from ~250 kg/mm^2 at the tip down to a value of ~170 kg/mm^2 at a distance of ~15 mm from the tip of the wedge sample (full circles in Figure 3). The higher hardness at the tip of the wedge (~250 kg/mm^2) is probably a result of carbide precipitates within grains (an indication supporting this interpretation was observed by the XRD in Figure 2(c)). A hardness value of ~170 kg/mm^2 corresponds to that of the ferrite phase. In contrast to the increased hardness in the bulk of the ferrite grains toward the tip region of the sample, the hardness of the precipitates at the grain boundaries decreases from ~450 to ~300 kg/mm^2 from the top to the tip of the wedge sample (open circle in Figure 3). The value of ~450 kg/mm^2 is in the range of the reported hardness value for the martensite,[16] while the value of ~300 kg/mm^2 is in the range of the values reported for the austenite.

C. *Shape and Size of the Ferrite Grains*

Figures 4(a) through (c) show two sets of optical micrographs taken from two perpendicular sections of the wedge sample, *i.e.*, *z*-*y* section (Figures 4(a)) and *z*-*x* sections (Figures 4(b) and (c)). Owing to the fact that the removal of heat from the solidified material is conducted mainly into the *y* direction (Figure 1), the appearance of the matrix grains is an elongated morphology in the *x*-*z* section, whereas in the *z*-*y* section, the ferrite grains show a polygonal morphology. These observations demonstrate that the wedge sample consists of columnar grain structure with a polygonal cross section. This kind of grain morphology was previously observed in a 12Cr-Mo-V steel melt-spun sample.[13]

With regard to the cooling rate effect on the grain size, Figure 4 clearly shows that the grain size decreases with increasing the cooling rate. At the very tip, in which the cooling rate is the highest, grain sizes were found to be less than 5 μm. In order to establish the relation between the ferrite grain size and the cooling rate, the grain sizes were measured by dividing the wedge sample into four regions corresponding to distances of 0 to 10, 30 to 40, 50 to 60, and 70 to 80 mm from the tip, respectively. The grain size obtained from each region is plotted in Figure 5 as a function of the average local cooling rate, *i.e.*, at distances of 5, 35, 55, and 75 mm from the tip. The average cooling rate was calculated by taking the average cooling rate at the lower and the higher distance of each measurement position. It is seen that the grain size decreases progressively with increasing cooling rate. The empirical relationship between the

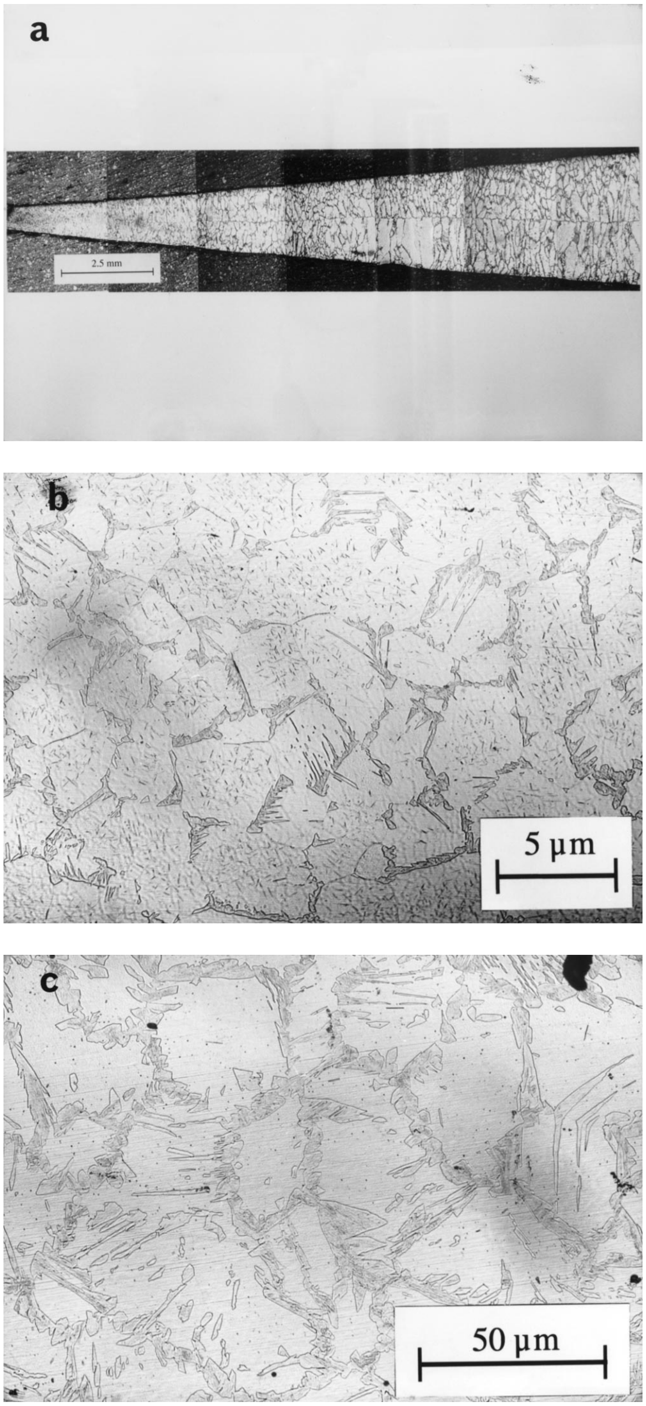

Fig. 4—(*a*) through (*c*) Optical micrographs showing the grains at (a) normal to *x*-axes and normal to the *y*-axes at (b) 0 to 10 mm and (c) 30 to 50 mm from the tip.

grain size, d_0 (μm), and the local cooling rate for this type of steel can be expressed as

$$d_0 = \frac{(804\ \mu\text{m}\ (\text{K/s})^{0.4})}{\dot{T}^{0.4}} \qquad [2]$$

The measured grain sizes, *i.e.*, about 60 grain measured for each region, varied along the *z* direction (Figure 1). Error bars in Figure 5 reproduce this variation.

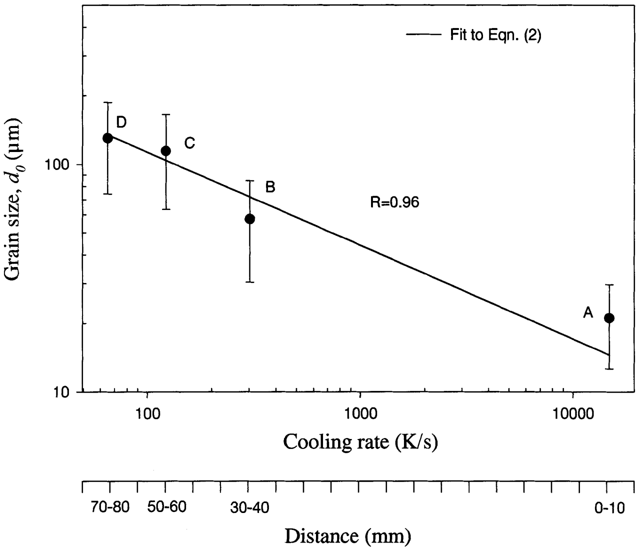

Fig. 5—The grain sizes *vs* the average cooling rate. The measurements were conducted at different locations within the wedge-formed sample (A) at 0 to 10 mm, (B) at 30 to 40 mm, (C) at 50 to 60 mm, and (D) at 70 to 80 mm. The fitting parameter, *R*, is found to be 0.96.

D. *Precipitation at the Ferrite Grain Boundaries*

As seen in Figure 4, the precipitation of the second phases occurred either at the ferrite grain boundaries or within the grains. The former is observed along the entire wedge sample and will be characterized in this section; the latter is found only within a distance of about 12 mm from the tip and will be described in Section E.

1. *Optical microscopy and TEM observations of the morphology*

Observations along the wedge-formed sample indicated that a significant change in the precipitate morphology exists. Figure 4 provides examples of the effect of increasing cooling rates, *i.e.*, different parts of the sample, on the morphologies. At the lower part of the sample, which is characterized by high cooling rates (*e.g.*, higher than 3.7×10^3 K/s), various morphologies have been observed: (1) grain boundary allotriomorphs, (2) grain boundary film, (3) primary side plate, (4) primary sawteeth, (5) thin film, and (5) isolated particles of second phase. Examples of optical microscopy micrographs of these morphology variations are shown in Figures 6(a) through (d). The labels in these micrographs correspond to "a" grain boundary allotriomorphs (Figure 6(a)), "b" grain boundary film (Figure 6(b)), "c" primary side plate (Figure 6(c)), and "d" primary sawteeth (Figure 6(d)). The morphologies observed by optical microscopy (OM) were later confirmed by TEM investigations, and examples of the observed morphologies are shown in Figures 7(a) through (c). Again, these observed morphologies indicate the existence of grain boundary allotriomorphs (Figure 7(a)), primary sawteeth (Figure 7(b)), and isolated austenite at the triple points (Figure 7(c)). Note that the primary sawteeth formed at the early stage of the transformation individually on the ferrite grain boundary, as seen from Figure 7(b) (also Figure 6(d)).

Besides the observed small isolated particles, which were found initially to nucleate at the grain corners, the initial stage of the nucleation of austenite was also observed to

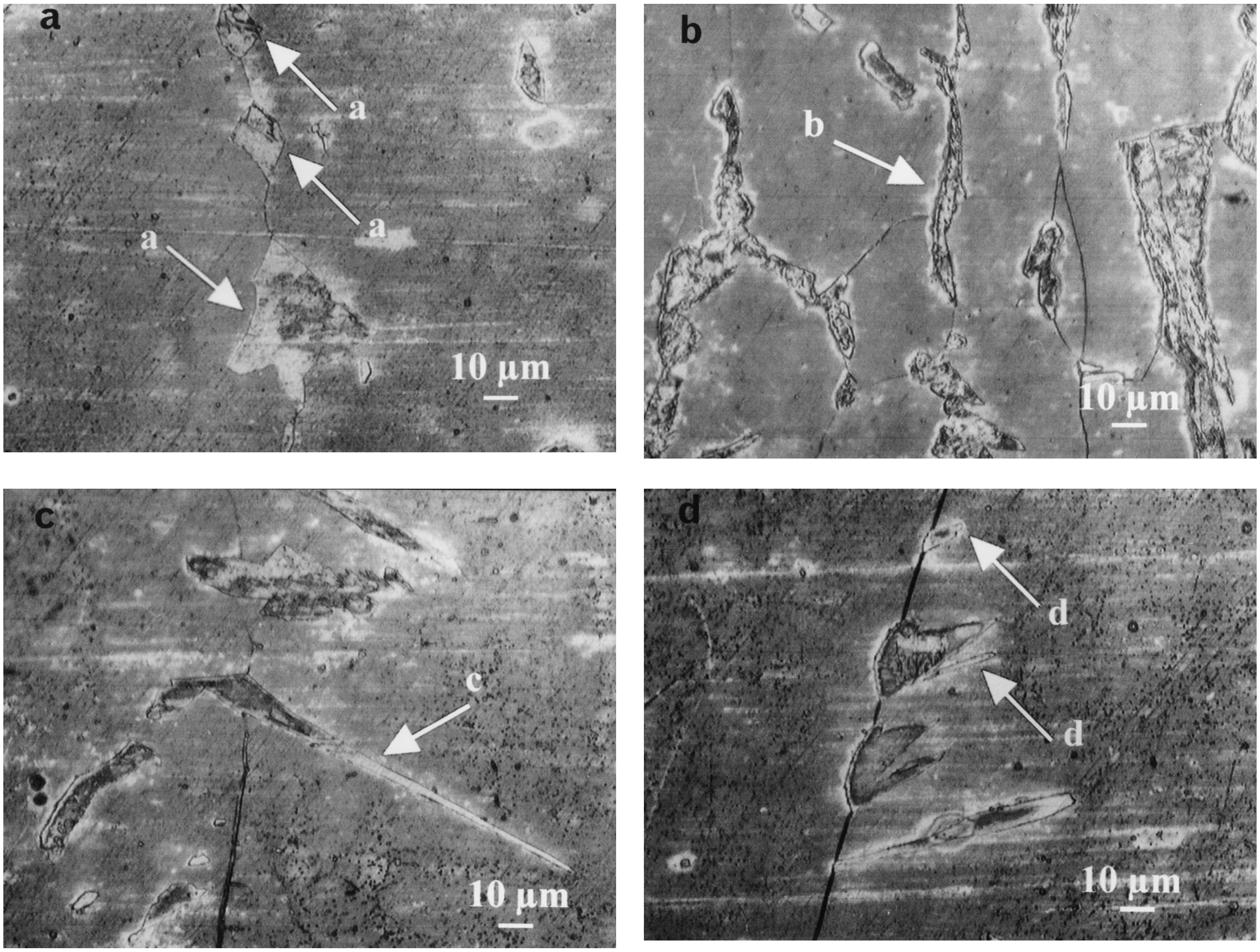

Fig. 6—Optical micrographs of the precipitate mophology at the lower part of the wedge sample: (*a*) allotriomorph structure, (*b*) grain boundary film, (*c*) primary sideplates, and (*d*) primary sawtheeth.

take place at the grain boundaries (Figure 8). In such cases, the austenite appeared as primary sideplates "a" and the initial stage of what are known as grain boundaries allotriomorphs "b" and "c" (Figure 8).

At the upper part of the sample, the Widmanstätten structure is well developed and covers the ferrite grain boundaries (*e.g.*, Figure 4). At this part of the sample, which corresponds to a later stage of the Widmanstätten development, the δ-ferrite grain sizes are coarser (Figures 4(a) and (b) and (c)). Figures 9(a) and (b) show optical micrographs at this stage of the Widmanstätten structure development. As seen in Figure 9(a), the secondary sideplates are found to grow from the allotriomorph structure (Figure 6(a)) or from a film structure (Figure 6(b)) into the ferritic matrix with fine secondary sideplates. Evidence for the formation of the Widmanstätten structure directly from the grain boundaries can be clearly seen in the early stage of the primary sideplate formation (Figure 6(c)) and at a later stage of the formation in Figure 9(b). In both figures, the primary sideplates are clearly shown to nucleate directly from the ferrite grain boundaries. The growth direction of the primary and secondary sideplates (Figures 9(a) and (b)) seems to be well defined, which implies that the grain crystallography determine the growth direction of these precipitates. Note that as the cooling rate decreases, the grains become coarser, leading to finer primary and secondary sideplates. The microstructure observed at this part of the wedge-shaped sample (zones "A" and "B") is found to be similar to the microstructure observed at a heat-treated Fe-25Cr-6Ni two-phase ($\alpha + \gamma$) stainless steel[17] in which austenite (γ) sideplates are found to grow from the γ film formed at the grain boundary into the ferrite (α) grains.

2. *Correlation between observed morphology and structure*

At the upper part of the sample, the austenite precipitated at high temperatures and transformed into martensite subsequent to its formation. The TEM evidence related to the internal structure of the Widmanstätten structure is shown in Figure 10, which reveals a clear substructure of martensite laths. This indicates that the solid-state cooling rates at this part of the wedge-formed sample were sufficiently high to allow a complete transformation of the austenite into martensite. In general, the lath spacing depends on the cooling rate and decreases with increasing cooling rate. Lath spacing of less than ~0.2 μm was found in this region (Figure 10), as a result of a high cooling rate.

In contrast to the complete transformation of austenite to martensite observed at the upper part, retained austenite was identified by XRD (Figure 2) at the tip region, although the

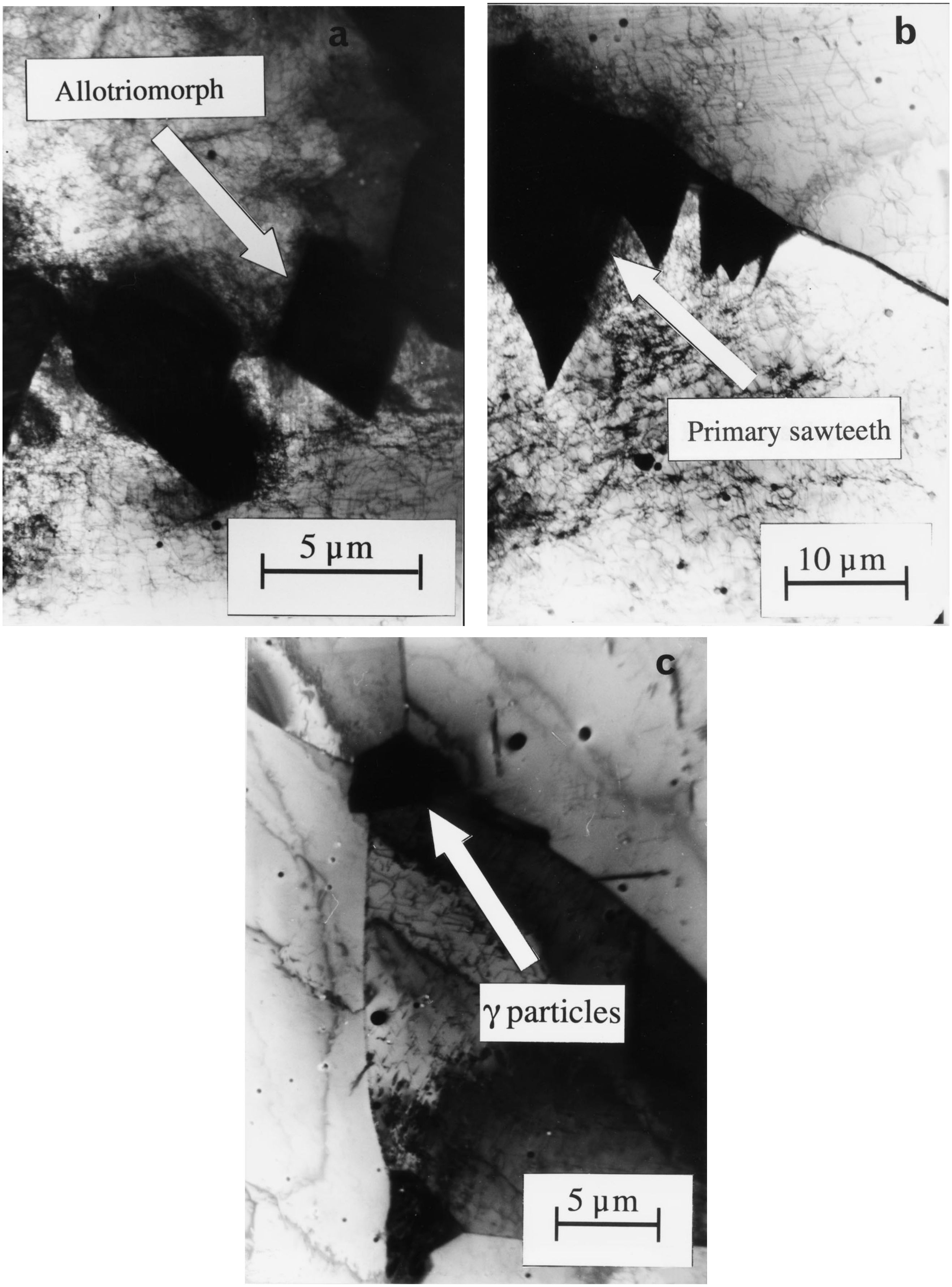

Fig. 7—(*a*) through (*c*) TEM micrographs of the precipitate morphology at the lower part of the wedge sample: (a) allotriomorph structure, (b) primary sideplates, and (c) isolated austenite particles.

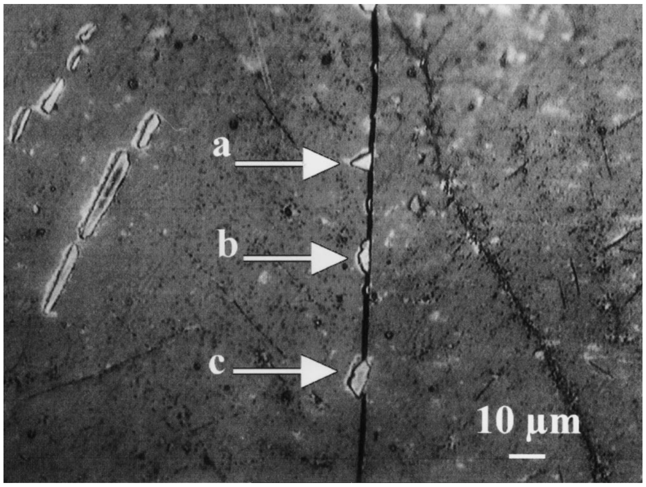

Fig. 8—Optical micrographs showing the initial growth stage of the austenite.

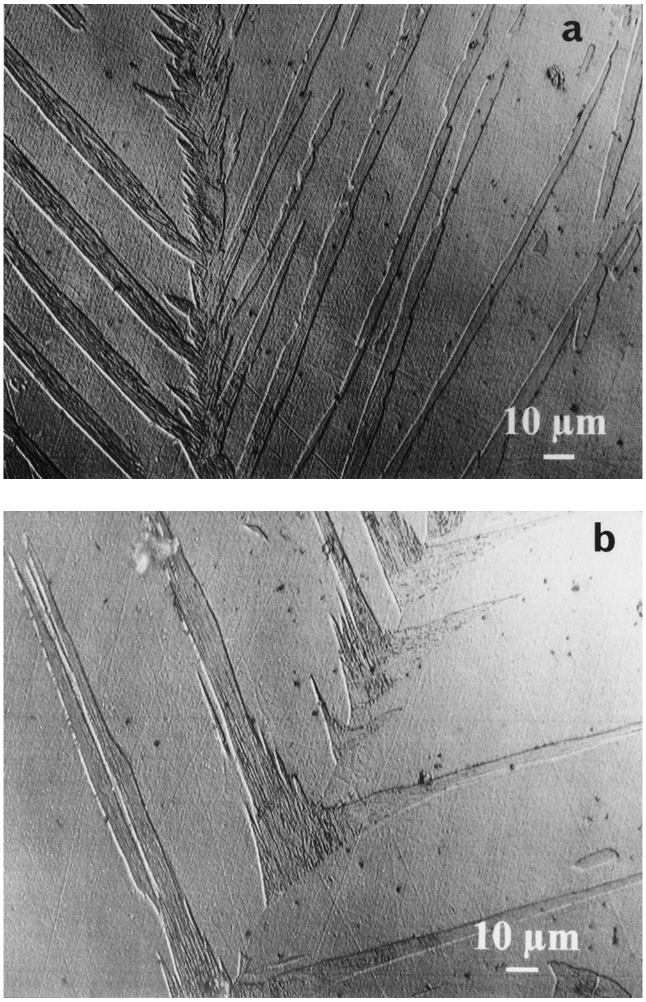

Fig. 9—(*a*) and (*b*) Optical micrographs showing the formation of secondary side plates: (a) secondary sideplates growing from the allotriomorph structure and (b) formation of the secondary sideplates directly from the grain boundaries.

solid-state cooling rate at this part is expected to be higher. To understand this, an effort was made to detect the austenite by the TEM. Morphological observations coupled with selected area electron diffraction patterns demonstrated that the retained austenite is restricted to the grain boundary precipitate particles of small sizes (<4 μm). In Figures 11(a) and (b), typical examples of retained austenite particles are shown. The correspondence between the particle size and the retention of austenite indicates an austenite size effect on the martensite transformation.

Fig. 10—TEM micrograph showing the characteristic lath of martensite.

E. *Precipitates within the Ferrite Grains*

At the lower part of the wedge-formed sample at a distance of about 12 mm from the tip, marked as "C" (Figure 1), besides the Widmanstätten martensite and the metastable austenite (which appeared as isolated precipitates of small sizes), a high density of needle-shaped precipitates, identified as cementite M_3C,[15] have been observed within the ferrite grains (Figure 4). Figure 12 shows a TEM montage of micrographs of the cementite precipitates, which were taken in the $[100]_\delta$ beam direction. The diffraction pattern of the cementite was indexed as $[3\bar{2}1]_c$. These observations are supported by the XRD observations (Figure 2(c)) in which evidence for the formation of carbide precipitates is observed as well as by the observed increase in the hardness close to the tip region (Figure 3).

It is seen that the precipitates have platelike shape rather than a needle shape, as viewed in optical microscopy (Figure 4). Detailed studies of the precipitate morphology[15,18] showed that the cementite is formed as fine needlelike

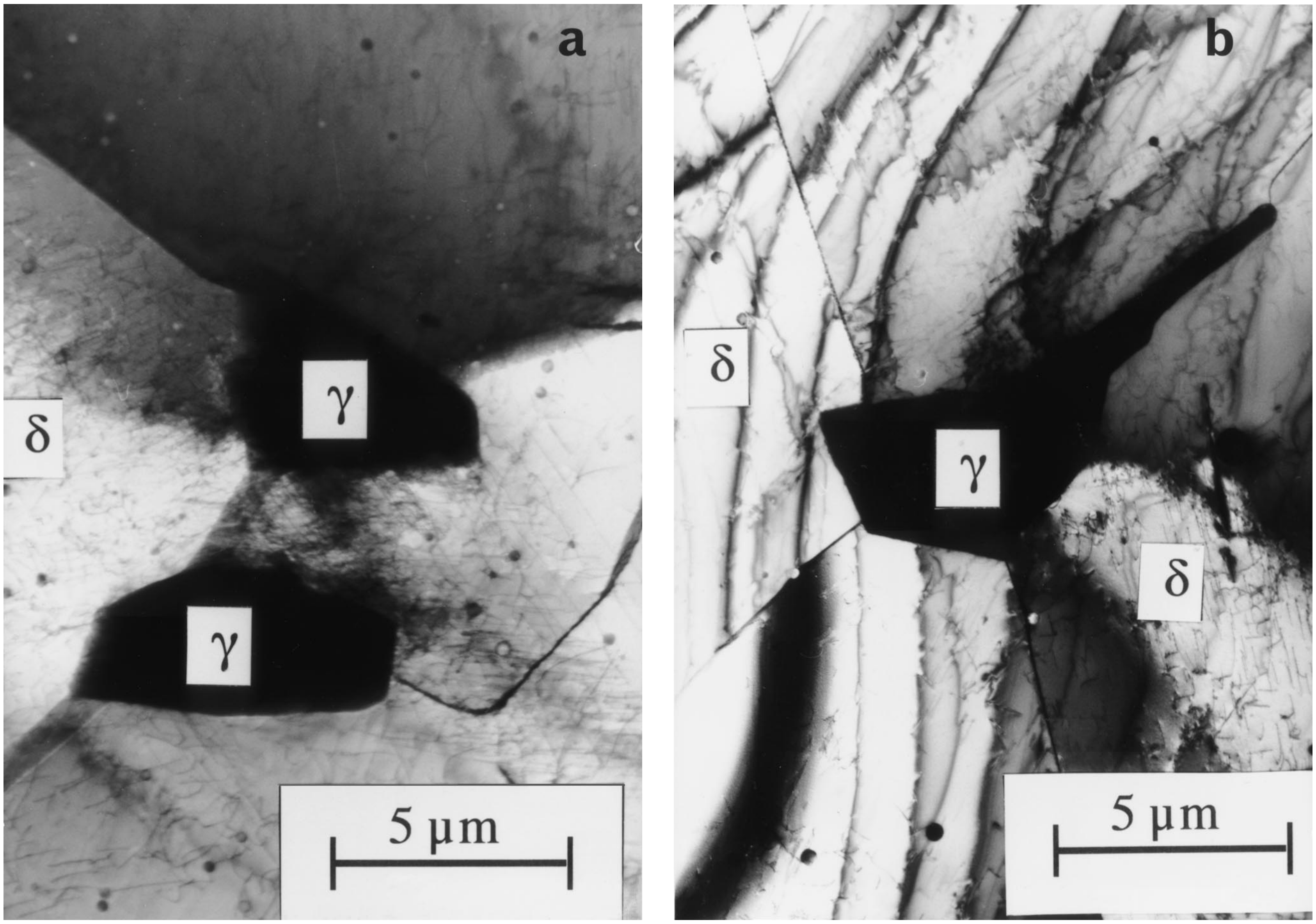

Fig. 11—(*a*) and (*b*) TEM micrographs taken from the tip of the wedge-formed sample showing the austenite nucleated at the triple point of grain boundaries. Key to symbols: (δ) ferrite and (γ) austenite.

precipitates joined together in a planar colony. Two directions of needles subtending an angle of about 70 deg characterize each colony. The needles grow almost equally, producing a planar structure of rectangle-shaped outline. It has been shown that the colonies are formed on the $\{100\}_c//\{011\}_\delta$ plans and that the growth directions of the precipitate needles in the colonies are $\langle 010\rangle_c//\langle 111\rangle_\delta$,[15] where the subscripts c and δ correspond to cementite and delta ferrite, respectively.

The effect of grain size and cooling rate on the precipitate length has been investigated and is illustrated in Figures 13(a) through (c). As seen from these figures, it is evident that the length of the precipitates increases with increasing grain size up to a distance of $\sim$12 mm away from the tip, at which point they disappear.

In the vicinity of some ferrite grain boundaries, precipitate-free zones (PFZs) were observed. Examples of OM and TEM observations of the PFZs are shown in Figures 14 and 15, respectively. It was found that the PFZs are always associated with the grain boundaries in which the austenite (martensite) had formed, suggesting that the reason for the PFZs is the nucleation and growth of grain boundary austenite during transformation. Note the high dislocation density in the PFZ (Figure 15) compared to that in the grain interior where the carbide precipitates are observed.

IV. DISCUSSIONS

A. *The Evolution of the Morphology*

The fact that the wedge-formed sample contained a large range of cooling rates provides the possibility to relate the evolution of the morphology described previously (Section D) to the different stages of the Widmanstätten structure formation.

The high cooling rates at the tip region result in formation of fine δ-ferrite grains with a polygonal shape. These fine grains allow the nucleation and growth of austenite to take place initially at the grain corners as fine isolated particles (*e.g.*, the arrow marked "a" in Figure 6(a) or Figure 7(c)). As demonstrated by TEM (Figure 11), the retained austenite is only related to the grain boundary precipitate particles of small sizes ($<$4 μm). However, the austenite particles nucleate initially not only at the grain corners but also at the grain boundaries (Figure 8). The nucleation of austenite in these particular sites is attributed to the low energy barrier for austenite nucleation, which is associated with the triple point[19] and low-angle grain boundary.[6] The high cooling rate in this region ensures that the sample will not remain for a long enough time at high temperature to permit a significant growth of the austenite particles into Widmanstätten structure. The austenite at this early stage of the transfor-

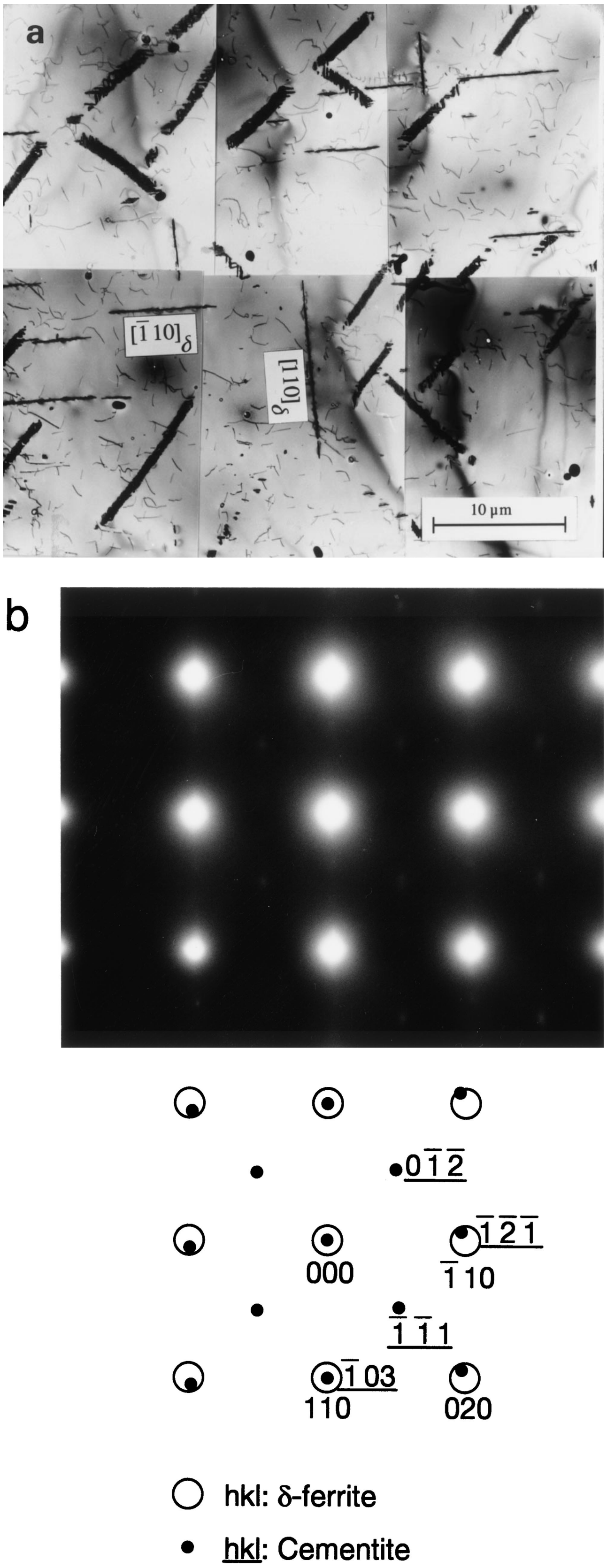

Fig. 12—(*a*) TEM montage of the precipitate morphology and (*b*) the corresponding diffraction pattern, which is indexed as $[001]_\delta//[3\bar{2}1]_c$. The precipitates are formed on the $\{\underline{1}10\}_\delta$ habit planes. These precipitates, which are formed on $(110)_\delta$ and $(\bar{1}10)_\delta$, are viewed edge-on in the beam direction used.

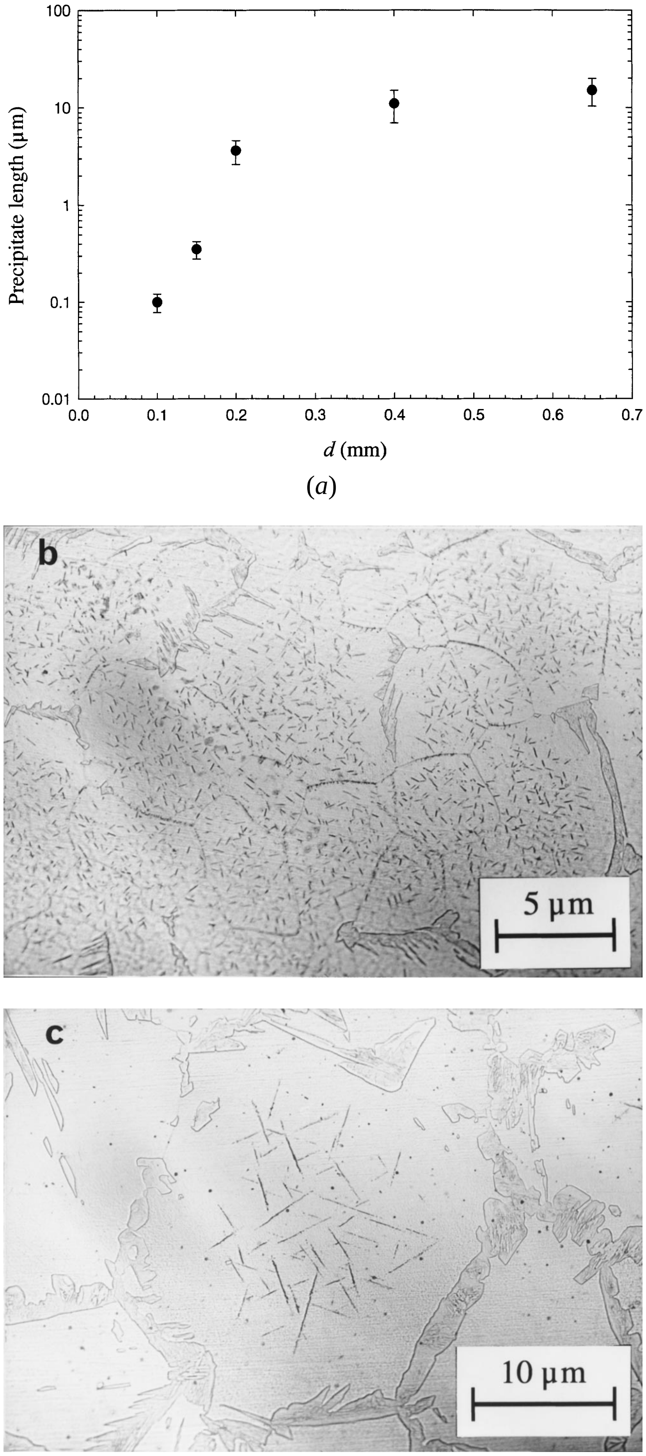

Fig. 13—(*a*) The length of the cementite precipitates at different parts of the wedge as well as micrographs showing the precipitate lengths at different locations within the wedge; (b) $d = 0.16$ mm and (c) $d = 0.2$ mm.

mation takes the form of different types of morphologies (Figures 6 and 7): (1) grain boundary, allotriomorphs, (2) grain boundary film, (3) primary side plate, (4) primary sawteeth, and (5) isolated particles of second phase.

Based on these observations, we can conclude that such a variation in morphology observed at the lower part of the wedge-formed sample reflects the nucleation and growth of

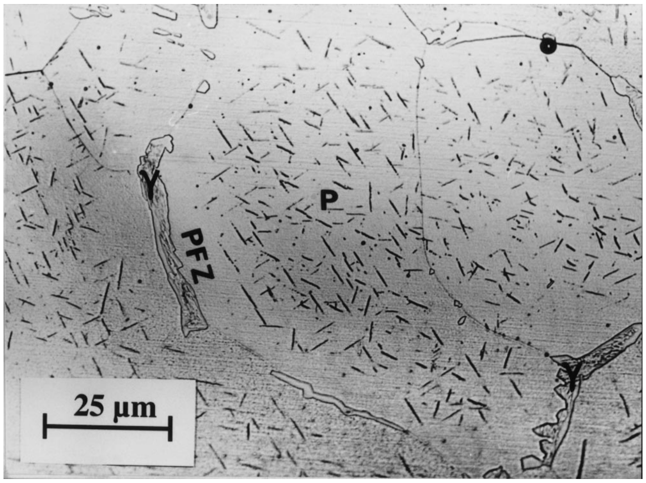

Fig. 14—Optical micrograph of the PFZ around the austenite.

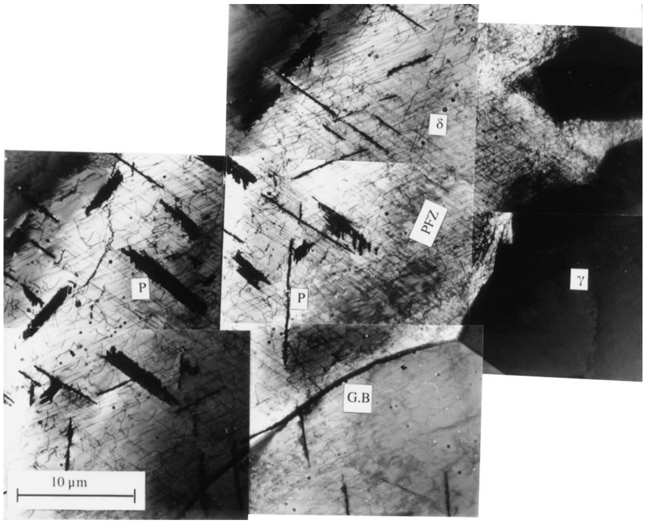

Fig. 15—TEM montage of the precipitate area depleted with precipitates as marked by arrows. Note that the PFZ, as shown in this figure, is characterized by high dislocation density around the austenite.

the austenite precipitates at the initial stage of the Widmanstätten structure. The formation of fine isolated particles of retained austenite at this part of the sample is attributed to the effect of rapid cooling. The fine grain sizes in this region are also attributed to the effect of high cooling rate. Grain sizes as fine as 5 to 20 μm were observed at a d of < 500 μm. These fine grain sizes reflect the high cooling rate in this area, $> 3.7 \times 10^3$ K/s.

At a later stage of the transformation at the upper part of the sample, the Widmanstätten structure is fully formed. The Widmanstätten precipitates can be described as plates or needles growing either directly from the matrix grain boundaries (primary sidplates) or from grain boundary precipitates (secondary sideplates) or with no interconnectivity at all (intragranular).[7] The latter was found recently by Kral and Spanos[7] not to be a real morphology but an effect of two-dimensional sectioning. A detailed investigation of the proeutectoid ferritic steel indicates that the secondary sideplates formed by two mechanisms.[20,21] The first is sympathetic nucleation at ferrite allotriomorphs and the second is lateral impingement of primary sideplates developed directly from the austenite grain boundaries by individual nucleation events. Evidence of these two mechanisms has been observed in the present work: the formation of the secondary sideplates from allotriomorphs (Figure 9(a)) and the formation of the primary sideplates directly from the ferrite grain boundary (Figures 6(c) and 9 (b)). It should be recognized that sympathetic nucleation is defined as the nucleation of a precipitate crystal at the interface boundary of another crystal of the same phase when both crystals differ in composition from the matrix.[20] As such, it is difficult to judge from Figure 9(a) whether the secondary sidplates where sympathetically nucleated on the grain boundary ferrite allotriomorphs.

B. *Stabilization of the Austenite*

The correspondence between the particle size and the retention of austenite observed in the present investigation indicates an austenite size effect on the martensite transformation. Such an austenite size effect has been previously observed for the Cu-2 wt pct Fe, Cu-1 wt pct Fe,[22,23] and Cu-Fe-Co alloys[24] and for nanoscale particles of Fe-Ni.[25] Investigations for the Cu-Fe alloys showed that the fcc precipitates of size 20 to 30 nm do not transform to the martensite phase on cooling. The coherency of the precipitates with the matrix is the main factor determining the martensitic transformation. Easterling and Miekk-Oja[22] have shown that nucleation that occurs homogeneously leads to fully coherent spherical fcc precipitates; however, with prolonged annealing time, the fcc precipitates grow, lose their coherency, and take the cubic form. Lin *et al.*,[24] for the Cu-Fe-Co system, have also pointed out the dependence of the martensitic transformation driving force on the variation of the precipitate composition with particle size; *i.e.*, any deviation from 33 wt pct Co decreases the driving force for the fcc-to-bcc transformation. In the nanoscale particles of the Fe-Ni system,[25] the fcc is found to become more stable when the size is reduced, *e.g.*, the specimens that were composed of grains smaller than 5 nm in size were expected to consist of bcc and martensite; however, the austenite is the only phase observed to be formed. The origin of austenite stabilization in these small grain sizes remains unclear. The martensite transformation in Fe-Ni powder particles has been previously studied by Cech and Turnbull[26] and more recently for a 12Cr-Mo-V steel.[12] In both studies, the dependence of the powder particle sizes on the relative fraction that transformed to martensite was found, *i.e.*, the martensite fraction decreases with decreasing particle size. In Reference 12, analysis of the rapidly solidified powders showed that when the size of the powder particles is smaller than a critical value of ~ 60 μm, the austenite formed within the ferrite powder particles cannot be transformed into martensite and is retained as austenite to room temperature. In this range of powder particle sizes, the grain size within the powder was found to be < 5 μm. The retained austenite precipitate sizes, therefore, are expected to be much smaller than this grain size due to the small amount of austenite. In other words, the austenite size in this case is smaller than the austenite particle sizes found in the present study (< 4 μm).

In contrary to the preceding reported data, the austenite particle sizes observed in the present investigation are much larger in fact by a factor of ~ 130. The question that is

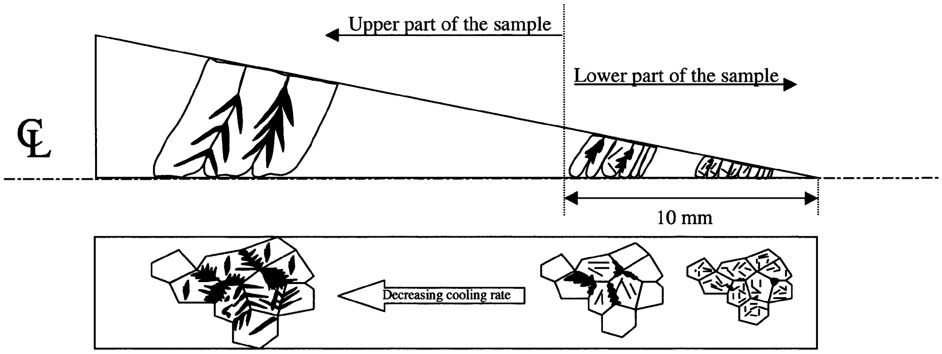

Fig. 16—Schematic diagram illustrating the different morphologies and structures observed at different parts of the wedge-formed sample (normal to the x and y axes).

Table II. The Morphologies and the Structures Evolution at Different Part of the Wedge-formed Sample.

d* (mm)	Cooling Rate (K/s)	Phases	Morphologies	Solidification Path
0 to 0.5 mm	>3700	δ, γ, Fe_3C, M	columnar δ grains, early stage of the Widmanstätten morphologies, cementite, isolated austenite particles, martensite	$L \rightarrow L + \delta \rightarrow L + \delta + \gamma \rightarrow \delta + M + \gamma^* + Fe_3C$
0.5 to 5 mm	3700 to 368	δ, M	columnar δ grains, later stage of the Widmanstätten martensite	$L \rightarrow L + \delta \rightarrow L + \delta + \gamma \rightarrow \delta + M$

*d is the half-distance (Fig. 1).

then raised is what is the reason for the stabilization of the austenite and the suspension of the martensite transformation? Martensitic transformation is typically a heterogeneous process in which the nucleation occurs on defects, *i.e.*, structure imperfections, in the parent phase, the austenite.[24] However, in small particle experiments,[26] the role of autocatalytic nucleation can be avoided. The probability of finding a heterogeneous site in a particle increases with increasing particle size. Bearing this in mind, in the large austenite particles, which probably contain more structure imperfections, it is easy for the martensite to nucleate; *e.g.*, evidence of this can be seen by the complete transformation of austenite into martensite at the upper part of the wedge (Figures 2(a) and (b)). The small particle sizes, on the other hand, contained less nucleation sites for martensite; in such a case, the martensite transformation is suppressed and the austenite retained to room temperature (*e.g.*, Figures 2(c) and 11(a) and (b)).

C. *The Evolution of the Microstructure*

The constitution of stainless steels is often predicted by the use of the Schaefler diagram,[27] which shows the phase fields in terms of Ni and Cr equivalent for the steel. Calculations of the Ni and Cr equivalents for the present steel indicate that the microstructures should contain a mixture of delta ferrite and martensite after cooling. The initial phase, which nucleated at the ferrite grain boundaries, is the austenite. During subsequent cooling, the austenite transformed into martensite (Figures 2(a) and (b) and 3). The identification of the phases demonstrated that the constituents observed at the upper part of the wedge sample are consistent with the prediction of the Schaefler diagram. However, deviations occur at higher cooling rates in which retained austenite (Figures 2(c) and 11) and intergranular precipitates of cementite M_3C (Figures 2(c) and 12) were observed. These morphological observations were supported by XRD, microhardness, and selected area electron diffraction pattern (Figures 2 and 3 and Reference 15). The decrease in the hardness at the grain boundary precipitates (the tip of the sample) is a consequence of the lower concentration of martensite and the retention of austenite at this part of the sample. The hardness value of $\sim$300 kg/mm^2 is in the range of the values reported for the austenite. The fine substructure of the Widmanstätten, *i.e.*, lath martensite ($\sim$0.2 μm), observed in this part of the sample (Figure 10), is also attributed to the rapid cooling in this area. The lath martensite was previously found in other rapid solidification processes, *e.g.*, for the Fe-Mo-C alloy[28] and for the Fe-Cr-C alloy.[13] In the latter case, the lath martensite dimensions were found to vary between 0.2 and 0.4 μm for cooling rates of $\sim 10^6$ K/s.

The carbon concentration of δ-ferrite is of principal importance in determining the kinetics of carbide formation. During cooling, two mechanisms by which the excess carbon in the ferrite is removed can take place simultaneously. One is the diffusion of carbon into the Widmanstätten austenite nucleated at the ferrite grain boundaries and the other is the precipitation of carbides within the ferrite. Each one of these two mechanisms may dominate, depending on the cooling rate, *i.e.*, location in the sample. At the tip of the sample, which is characterized by fine grain ferrite, only a few nuclei of austenite were formed on the grain boundaries. In such a case, the carbon concentration within the grains is relatively high and uniform. The high carbon concentration and the formation of high density of dislocations in this area promote the formation of a large amount of fine homogeneously distributed carbide precipitates (Figure 13(a)).[15]

As the grain size gradually increases with decreasing cooling rate, the amount of austenite precipitation at the grain boundaries increases, and this is accompanied by a reduction of the carbon concentration at the middle of the grains. This effect together with a low cooling rate, *i.e.*, longer time for the diffusion process to take place, at this region leads to a small volume fraction of large carbide precipitates (Figure 13(c)). Eventually, after a certain distance from the tip, the secondary sideplates further develop and surround the entire grain boundaries. In such a case, all the excess carbon content in the ferrite is removed by the formation of the austenite, and as a consequence, no carbide precipitates are formed above this distance.

The competition between the diffusion of carbon into the austenite and the formation of carbide precipitates led to the formation of PFZ at the grain boundaries where austenite had developed. The PFZ at the periphery of the high-temperature austenite resulted from the preferential removal of carbon by austenite. The formation of austenite, therefore, is the main reason for the depletion of carbon in this area. Simultaneously, the carbon level in the ferritic matrix is reduced considerably by the formation of carbides. Evidence to this can be seen by the formation of PFZ at the vicinity of the austenite, while no PFZ exists around the grain boundaries without austenite (Figure 15). Note that the formation of the PFZs has a large effect on the properties of the materials, *e.g.*, softens the material.[29] Based on the overall investigations, the solidification microstructure evolution along the sample is summarized in Figure 16 and Table II.

V. CONCLUSIONS

In order to study the cooling rate effect on the microstructures formed during solidification of a low-alloy 12Cr pct steel, a wedge-formed sample has been prepared by casting the base material into a wedge copper mold. A large cooling rate range of 40 to 10^5 K s^{-1}, therefore, has been achieved along the wedge-formed sample. A strong cooling rate effect on the phase constitution, grain size, morphologies, and sizes of the precipitates has been observed. The main results can be summarized as follows.

1. The matrix phase was invariably identified as ferrite over the entire cooling rate range; however, the ferrite grain size was found to decrease with an increase in the cooling rate. Grain sizes less than 5 μm were obtained at the very tip of the wedge sample where the cooling rate is highest.
2. Grain boundary precipitates were observed along the entire wedge-shaped sample; however, their amount increases gradually from the tip toward the top of the sample, associated with a gradual change in the morphology, *i.e.*, from an isolated particle nucleated at the grain corner or grain boundaries to a well-formed Widmanstätten structure. The essential structure of the grain boundary precipitates was identified as martensite, which is a result of the solid-state transformation product of high-temperature austenite. However, retained austenite was identified at the tip region (10 mm from the tip), which experienced high cooling rates ($>3.7 \times 10^3$ K s^{-1}).
3. Dispersed carbide precipitates within the ferrite grains were also observed at the tip region. The size of the carbides decreases but their density increases with increasing cooling rate.
4. The precipitation of austenite at the grain boundaries and the precipitation of carbides within the ferrite are considered as two competitive processes by which the excess of carbon in the solidified delta ferrite grains is removed. Depending on the cooling rate, one of these processes can dominate, resulting in the formation of different phases at different parts of the wedge-formed sample.

ACKNOWLEDGMENTS

The authors thank Drs. A.S. Petersen and J. Bilde-Sørensen and Professor J. Wert for reading the manuscript and for helpful discussions.

REFERENCES

1. E.A. Little, D.R. Harries, F.B. Pickering, and S.R. Keown: *Met. Technol.*, 1977, vol. 4, p. 205.
2. D.J. Gooch: *Met. Sci.*, 1982, vol. 16, p. 79.
3. R.R. Petri, E. Schnabel, and P. Schwaab: *Arch. Eisenhüttenwes.*, 1980, vol. 51, p. 335.
4. R.R. Petri, E. Schnabel, and P. Schwaab: *Arch. Eisenhüttenwes.*, 1981, vol. 52, p. 27.
5. C.A. Dubé, H.I. Aaronson, and R.F. Mehl: *Rev. Métall.*, 1958, vol. 55, p. 201
6. H.I. Aaronson: in *The Decomposition of Austenite by Diffusional Processes*, V.F. Zackay and H.I. Aaronson, eds., Interscience, New York, NY, 1962, p. 387.
7. M.V. Kral and G. Spanos: *Acta Mater.*, 1999, vol. 47, p. 711.
8. R.K.W. Honeycombe: *Steel: Microstructure and Properties*, Edward Arnold, London, 1981.
9. J.V. Wood and R.W.K. Honeycombe: *Phil. Mag. A*, 1978, vol. 37, p. 501.
10. C.N. Elliot, H.A. Davies, and G.W. Greenwood: *Mater. Sci. Eng.*, 1988, vol. 98, p. 285.
11. K. Ozbaysal and O.T. Inal: *Mater. Sci. Eng. A*, 1990, vol. 130, p. 205.
12. N.H. Pryds: Ph.D. Thesis, Risø National Laboratory, Roskilde, Denmark, Mar. 1997.
13. N.H. Pryds, E. Johnson, S. Linderoth, and A.S. Pedersen: *Metall. Mater. Trans. A*, 1998, vol. 29A, pp. 367-76.
14. N.H. Pryds, T. Juhl, and A.S. Pedersen: *Metall. Mater. Trans. A*, 1999, vol. 30A, pp. 1817-26.
15. X. Huang and N.H. Pryds: *Acta Mater*, in press.
16. D.R. Barraclough and D.J. Gooch: *Mater. Sci. Technol.*, 1985, vol. 1, p. 961.
17. K. Ameyama, T. Maki, and I. Tamura: *J. Jpn Inst. Met.*, 1986, vol. 50, p. 10.
18. N.H. Pryds and X. Huang: *Scripta Mater.*, 1997, vol. 36, p. 1219.
19. G. Thewlis: *Mater. Sci. Technol.*, 1994, vol. 110.
20. H.I. Aaronson, G. Spanos, R.A. Masamura, R.G. Vardiman, D.W. Moon, E.S.K. Menon, and M.G. Hall: *Mater. Sci. Eng.*, 1995, vol. B32, pp. 107-23.
21. G. Spanos and M.G. Hall: *Metall. Mater. Trans. A*, 1996, vol. 27A, pp. 1517-23.
22. K.E. Easterling and H.M. Miekk-Oja: *Acta Metall.*, 1967, vol. 15, p. 1133.
23. K.E. Easterling and G.C. Weatherly: *Acta Metall.*, 1969, vol. 17, p. 845.
24. M. Lin, G.B. Olson, and M. Cohen: *Acta Metall. Mater.*, 1993, vol. 41, p. 253
25. T. Tadaki, Y. Murai, A. Koreeda, Y. Nakata, and Y. Hirotsu: *Mater. Sci. Eng. A*, 1996, vol. 217–218, p. 235.
26. R.E. Cech and D. Turnbull: *Trans. AIME*, 1956, vol. 206, p. 124.
27. A.L. Schaeffler: *Met. Progr.*, 1949, vol. 56, pp. 680 and 680B.
28. J. Zboril and Z. Posedel: *Z Metallkd.*, 1970, vol. 61, p. 214.
29. R. Maldonado and E. Nembach: *Acta Mater.*, 1997, vol. 45, p. 213.